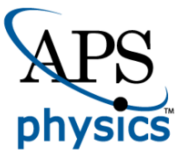

Nanoscale imaging of magnetization reversal driven by spin-orbit torque

Ian Gilbert, P. J. Chen, Daniel B. Gopman, Andrew L. Balk, Daniel T. Pierce, Mark D. Stiles, and John Unguris

Phys. Rev. B **94**, 094429 — Published 23 September 2016

DOI: 10.1103/PhysRevB.94.094429

Nanoscale imaging of magnetization reversal driven by spin-orbit torque

Ian Gilbert[1,*], P.J. Chen[2], Daniel B. Gopman[2], Andrew L. Balk[1,3,4], Daniel T. Pierce[1], Mark D. Stiles[1], and John Unguris[1]

[1]*Center for Nanoscale Science and Technology, National Institute of Standards and Technology, Gaithersburg, MD 20899*
[2]*Materials Science and Engineering Division, National Institute of Standards and Technology, Gaithersburg, MD 20899*
[3]*Maryland NanoCenter, University of Maryland, College Park, MD 20742*
[4] *Los Alamos National Laboratory, Los Alamos, NM 87545*

We use scanning electron microscopy with polarization analysis to image deterministic, spin-orbit torque-driven magnetization reversal of in-plane magnetized CoFeB rectangles in zero applied magnetic field. The spin-orbit torque is generated by running a current through heavy metal microstrips, either Pt or Ta, upon which the CoFeB rectangles are deposited. We image the CoFeB magnetization before and after a current pulse to see the effect of spin-orbit torque on the magnetic nanostructure. The observed changes in magnetic structure can be complex, deviating significantly from a simple macrospin approximation, especially in larger elements. Overall, however, the directions of the magnetization reversal in the Pt and Ta devices are opposite, consistent with the opposite signs of the spin Hall angles of these materials. Our results elucidate the effects of current density, geometry, and magnetic domain structure on magnetization switching driven by spin-orbit torque.

I. INTRODUCTION

Efficient electrical control of magnetism enables spintronic devices such as magnetoresistive random access memory and is also of significant fundamental interest due to the diverse and complex physical mechanisms by which electric field and magnetization can couple [1,2]. Magnetization can be manipulated with electric field via coupled order parameters in multiferroics [3-5], strain in piezoelectric/ferromagnetic heterostructures [6,7], spin-transfer torque in ferromagnet/nonferromagnet/ferromagnet devices [8], and spin-orbit torques in heavy metal/ferromagnet [9-11] and topological insulator/ferromagnet [13,14] bilayers. Spin-orbit torques have been characterized by a large number of transport and ferromagnetic resonance (FMR) techniques [9,13-25], but to date all magnetic microscopy studies of magnetization reversal driven by spin-orbit torques have used magneto-optical Kerr effect (MOKE) microscopy [26-31], the resolution of which is diffraction-limited. Furthermore, these previous microscopy studies have considered only perpendicularly-magnetized ferromagnetic films, which provide higher MOKE contrast than in-plane magnetized samples. While these perpendicularly-magnetized systems are technologically relevant, they require symmetry breaking provided by some extra experimental parameter such as external magnetic field [26], exchange bias [25,30], or a special sample geometry [20,31] to generate deterministic magnetization switching. On the

other hand, in-plane magnetized devices can exhibit field-free deterministic switching, which makes them appealing from an applications perspective [9,23].

Here we describe scanning electron microscopy with polarization analysis (SEMPA) [32,33] measurements of field-free deterministic magnetization switching driven by the spin-orbit torques of Pt and Ta. SEMPA (illustrated schematically in Fig. S1) directly probes a sample's magnetization by measuring the spin polarization of emitted secondary electrons in a scanning electron microscope. SEMPA has superior spatial resolution to MOKE microscopy (down to 5 nm [34]), can quantitatively measure all three spatial components of magnetization, and has a probing depth of about 1 nm, making it a valuable tool for studying the nanoscale properties of magnetic thin films.

II. EXPERIMENTAL DETAILS

We study the simplest possible spin-orbit torque model system: a heavy metal/ferromagnet bilayer. Our samples (depicted in Fig. 1a and b) comprise a 2 nm thick $Co_{20}Fe_{60}B_{20}$ film patterned into rectangles ranging from 0.55 μm × 4.0 μm to 3.0 μm × 4.0 μm on top of 6 nm thick Pt or Ta strips (the long axis of the strip is parallel to the x-axis). This range of aspect ratios allows us to investigate the behavior of elements which are single-domain with mostly collinear magnetization as well as ones with significant domain structure. This comparison is of interest because many simulations of spin-orbit torque use the macrospin approximation, but in real devices, the magnetization structure may be more complex [35]. The shape anisotropy of the rectangles causes the overall in-plane magnetization (Figs. 1c and d and Supplementary Fig. 2) to point along ± y. When current flows through the heavy metal strip, the spin-orbit coupling generates a transverse spin current (as shown in Fig. 1b) in the ± z direction which exerts a torque on the adjacent CoFeB magnetization. This spin-orbit torque can be described as a magnetization-dependent effective field [36]

$$\mathbf{B}_{\mathrm{SOT}} = \frac{\hbar}{2e}\frac{j\theta_{\mathrm{SH}}}{tM_s}(\hat{\mathbf{z}} \times \hat{\mathbf{j}}) \times \hat{\mathbf{m}},$$

where j is the charge current density, θ_{SH} is the effective spin Hall angle, t is the thickness of the ferromagnetic layer, and M_s is the saturation magnetization. The substrate normal direction, current direction, and magnetization direction are given by $\hat{\mathbf{z}}$, $\hat{\mathbf{j}}$, and $\hat{\mathbf{m}}$, respectively. The spin Hall angles θ_{SH} of Pt and Ta have opposite signs [9-11], so while the spin-orbit torque of Pt has the same symmetry as the Oersted field, the spin-orbit torque of Ta has opposite symmetry, permitting the robust identification of spin-orbit torque-induced magnetization reversal.

Pt/CoFeB and Ta/CoFeB films were grown via sputter deposition. To avoid charging during SEMPA imaging, the films were grown on doped Si wafers with a native oxide layer. The film stacks were $Si/SiO_x/Pt(6)/Co_{20}Fe_{60}B_{20}(2)/Pt(2)$ and $Si/SiO_x/Ta(6)/Co_{20}Fe_{60}B_{20}(2)/Pt(2)$ (thickness in nm). The 2 nm Pt capping layer protects the CoFeB from oxidation during device fabrication. Deposition rates were 2.2 nm/min (Pt), 1.8 nm/min (Ta), and 3.5 nm/min (CoFeB). The instrument base pressure was 3×10^{-6} Pa. Vibrating sample magnetometry (VSM) measurements verified that the CoFeB magnetization lies in-plane, which is expected for thicknesses greater than about 1 nm [37,38]. The VSM hysteresis loops for the Pt and Ta samples are shown in Figs. 1c and d, respectively. The unpatterned films both had a coercivity of 9.3 mT.

From these films, devices similar to those of Ref. 25 were fabricated, comprising arrays of 20 parallel, 4 μm wide strips. Arrays of X(6)/CoFeB(2)/Pt(2) (X=Pt or Ta) wires were defined using a direct write laser system and Ar ion beam etching. A second step of lithography and Ar ion beam etching defined the transverse CoFeB rectangles, and a final step of lithography and electron beam evaporation was used to deposit Ti(10 nm)/Au(60 nm) contacts. These contacts were wire bonded to pads on a specialized sample stage connected to a pulse generator via electrical feedthroughs, enabling current pulses to be sent to the sample while it is mounted in the SEMPA. A scanning electron micrograph of an exemplary device is shown in Fig. 1a. The coercivity of the individual rectangles after patterning was determined to be 2 mT to 4.5 mT using MOKE (see Supplementary Fig. 2). Prior to imaging with SEMPA, the 2 nm Pt cap was removed with in-situ Ar ion etching, and a few monolayers of Fe were evaporated on top of the CoFeB to increase the magnetic contrast [39]. We then used SEMPA to image the magnetization configuration of the CoFeB before and after current pulses of length 0.3 μs were applied to the heavy metal strips.

III. RESULTS AND DISCUSSION

Figure 2 illustrates the central result of this paper. Figure 2a shows a SEMPA image of the magnetization configuration of six CoFeB rectangles on Pt strips (indicated by dashed lines) prior to a current pulse. The magnetization direction in the elements is denoted by color, keyed to the color wheel in the lower right corner, and by the overlaid arrows. The nonmagnetic areas surrounding the elements are blacked out for clarity. In Fig. 2a, the magnetization is initially set (by a previous current pulse) in the +y direction. Fig. 2b shows the same rectangles after a 0.3 μs, 3×10^{12} A/m^2 current pulse in the +x direction (note that throughout this work we describe the direction of positive current rather than electron flow). The magnetization has now reversed to point in the –y direction. We attribute this magnetization reversal to the spin-orbit torque exerted on the CoFeB by the underlying Pt strips. Fig. 2c and d show analogous SEMPA images of CoFeB rectangles on Ta strips. In this case, magnetization initially pointing in the –y direction is reversed to the +y direction by a 0.3 μs, 8×10^{11} A/m^2 current pulse in the +x direction. The images presented in Fig. 2 demonstrate the ability of high resolution magnetic microscopy to inform device design by providing a high-resolution magnetization map. The resolution of these images is based on a pixel size of 62 nm, an order of magnitude superior to than that obtained with MOKE microscopy. More details of the SEMPA images are presented in Supplementary Fig. 3.

While the Oersted field from the heavy metal strips approaches the magnitude of the coercivity of the unpatterned film and has the same symmetry as the switching observed in the Pt device, it cannot explain the opposite switching observed in the Ta device. This behavior is expected for the spin Hall effect, however, since the spin Hall angle of Ta is negative and opposite to that of Pt [9-11]. The CoFeB rectangles on the Ta wires also switch at a lower current density, which is consistent with the fact that the magnitude of the spin Hall angle in Ta is greater than that of Pt [10,11]. We emphasize that the magnetization reversal shown here is completely deterministic without the need for special sample fabrication techniques or an applied field to break symmetry. While applications-oriented devices based on spin-orbit torques may require more complicated geometries or switching protocols, the sample geometry described here is ideal for fundamental studies of spin-orbit torques because it includes only the components necessary for manipulating

magnetization: a heavy metal layer to supply the spin-orbit torque, and a ferromagnet layer to manipulate. One benefit of this sample design is that there is no need to apply a magnetic field to cancel the shift (dipolar) field produced by the fixed layer of a magnetic tunnel junction [9,23].

Interestingly, for both the Pt and the Ta samples, not only is the y component of the CoFeB magnetization reversed, but the magnetization components in the ±x directions are also consistently reversed. Most of the x-component magnetization switching here (and in Fig. 3) is deterministic, which is unexpected for conventional spin-orbit torque alone. Some degree of symmetry breaking is necessary to cause consistent switching of the x-component of magnetization. The stray field inside the microscope is < 0.1 mT and the rectangles lack structural asymmetry, but this behavior can be explained by a small in-plane anisotropy, which SEMPA imaging of a continuous region of Ta/CoFeB suggests is present (Supplementary Fig. 4). This anisotropy couples the x- and y-components of the magnetization and leads to deterministic switching for the x-component as well as the y-component.

One advantage of imaging studies of spin-orbit torques is that many devices can be characterized in parallel. We demonstrate this in Fig. 3, which shows magnetization reversal of 30 CoFeB elements on Ta wires. The images in Fig. 3 are difference images obtained by subtracting sequential SEMPA images of the x- and y- components of magnetization. In Fig. 3a and b, the magnetization of every element is switched from the +y direction to the –y direction and back by 8×10^{11} A/m^2 current pulses. Figs. 3c and d show the analogous changes in the x-component of magnetization. Figs. 3e and f show the y-component of the rectangles again, this time while a sequence of slightly smaller current pulses is applied. In this case, none of the 1 μm × 5 μm rectangles switch, and only parts of some of the wider rectangles' magnetization switch. While both the magnetic moment of a rectangle and the amount of spin current received from the underlying Ta strip scale with the area of the rectangle, the smaller rectangles have a greater shape anisotropy (due to their higher aspect ratio). Therefore, they require a larger spin-orbit torque, and consequently a slightly larger current, to switch. Also, the magnetization of the large rectangles can depart significantly from a uniform ± y configuration to a multidomain configuration, with the current only reversing part of the magnetization.

We took series of such images of many rectangles while applying current pulses of varying amplitude in order to determine the critical current for reversing the CoFeB magnetization. Over the course of these measurements, we switched the magnetization of each sample more than 10 times without damaging the samples. Each image was subtracted from the subsequent image to increase magnetic contrast and remove any non-magnetic background. The images were binarized using automatic thresholding routines (see Supplementary Fig. 5 for a comparison of the original and thesholded versions of the difference images), and the fraction of each rectangle's magnetization that reversed between each pair of images was then extracted. The results are presented in Fig. 4 and are not sensitive to the arbitrarily chosen thresholding parameters. Typical critical currents for switching were $(1.90 \pm 0.03) \cdot 10^{12}$ A/m^2 and $(6.74 \pm 0.04) \cdot 10^{11}$ A/m^2 for the Pt and Ta samples, respectively. These values are for the y-component of magnetization of the intermediate-sized rectangles, although the critical current did not strongly depend on the rectangle size. The x-component magnetization preferentially switches at the same critical current density as the y-component (to be parallel to the current in both samples, as shown in Supplementary Fig. 6). As previously discussed, because magnetization switching parallel to the current direction is stochastic in the absence of symmetry breaking (e.g., an applied magnetic field), these data suggest the presence of a small in-plane anisotropy in the

CoFeB film. The critical currents for the x- and y-components of magnetization of all the rectangles can be found in Supplementary Tables 1 and 2 and correspond to effective spin Hall angles of 0.03% and -0.07% for Pt and Ta, respectively.

While the exact value of the critical current depends on details such as the device interface [40,41] and the Oersted field [42], the smaller critical current in the Ta sample is qualitatively consistent with the larger magnitude of the spin Hall angle of Ta [10,11]. The magnitudes of the effective spin Hall angles measured here are much lower than others reported for similar device geometries [9,23]. This may be due to different reversal modes present in our larger CoFeB rectangles or to details of sample fabrication. The heavy metal strips were overetched when the Pt capping layer was removed, effectively reducing the amount of current flowing at the heavy metal/CoFeB interface (see Supplementary Fig. 7). Perhaps even more importantly, the Si/native oxide substrate shunts some of the current away from the heavy metal strips, causing an overestimate of the current producing spin-orbit torque and consequently an underestimate of the spin Hall angle. We emphasize that the SEMPA measurements described here do not represent an accurate means by which to measure spin Hall angles of Pt and Ta, though they do provide a detailed picture of the magnetization switching produced by spin-orbit torques of these materials.

IV. SUMMARY

We have used SEMPA to directly visualize magnetization reversal driven by the spin-orbit torques of Pt and Ta. In our in-plane magnetized Pt/CoFeB and Ta/CoFeB samples, the reversal is completely deterministic even in the absence of an applied magnetic field. Furthermore, the symmetry of the magnetization reversal is opposite for CoFeB rectangles placed on Pt and Ta strips, which cannot be explained by the Oersted field from the strip but which is expected for the spin Hall effect. The high resolution images of the magnetization allow us to resolve not only the overall magnetic moments of the ferromagnetic device elements, but also the subtle features of the non-uniform magnetization in the wider rectangles. These results highlight the role of magnetic microscopy as a complement to transport measurements and FMR in the design of spintronic devices utilizing spin-orbit torques including memory elements, racetrack memory [43,44], and skyrmion-based devices [36,45] and highlight the importance of simulations of spin-orbit torque that move beyond the simple macrospin approximation.

ACKNOLWEDGEMENTS

This project was supported by the National Institute of Standards and Technology, Center for Nanoscale Science and Technology under project numbers R13.0004.04 and N09.0017.07 (nanofabrication). I.G. acknowledges support from the National Research Council's Research Associateship Program. A.L.B. acknowledges support of this research under the Cooperative Research Agreement between the University of Maryland and the National Institute of Standards and Technology Center for Nanoscale Science and Technology, Award No. 70NANB10H193, through the University of Maryland. We thank Scott Crooker for assistance with the MOKE measurements.

*ian.gilbert@nist.gov

1. S.D. Bader and S.S.P. Parkin, *Annu. Rev. Condens. Matter Phys.* **1**, 71 (2010).
2. F. Matsukura, Y. Tokura, and H. Ohno, Control of magnetism by electric fields, *Nature Nanotech.* **11**, 209 (2015).
3. Y.-H. Chu, L.W. Martin, M.B. Holcomb, M. Gajek, S.-J. Han, Q. He, N. Balke, C.-H. Yang, D. Lee, W. Hu, Q. Zhan, P.-L. Yang, A. Fraile-Rodriguez, A. Scholl, S.X. Wang, and R. Ramesh, Electric-field control of local ferromagnetism using a magnetoelectric multiferroic, *Nature Mater.* **7**, 478 (2008).
4. J. Heron, J.L. Bosse, Q. He, Y. Gao, M. Trassin, L. Ye, J.D. Clarkson, C. Wang, J. Liu, S. Salahuddin, D.C. Ralph, D.G. Schlom, J. Iñiguez, B.D.Huey, and R. Ramesh, Deterministic switching of ferromagnetism at room temperature using an electric field, *Nature* **516**, 370 (2014).
5. R. Ramesh and N.A. Spaldin, Multiferroics: progress and prospects in thin films, *Nature Mater.* **6**, 21 (2007).
6. M. Buzzi, R.V. Chopdekar, J.L. Hockel, A. Bur, T. Wu, N. Pilet, P. Warnicke, G.P. Carman, L.J. Heyderman, and F. Nolting, Single domain spin manipulation by electric fields in strain coupled artificial multiferroics nanostructures, *Phys. Rev. Lett.* **111,** 027204 (2013).
7. A.T. Chen and Y.G. Zhao, Research update: Electrical manipulation of magnetism through strain-mediated magnetoelectric coupling in multiferroic heterostructures, *APL Mat.* **4**, 032303 (2016).
8. D.C. Ralph and M.D. Stiles, Spin transfer torques, *J. Magn. Magn. Mater.* **320**, 1190 (2008).
9. L. Liu, C.-F. Pai, Y. Li, H.W. Tseng, D.C. Ralph, and R.A. Buhrman, Spin-torque switching with the giant spin Hall effect of tantalum, *Science* **336**, 555 (2012).
10. J. Sinova, S.O. Valenzuela, J. Wunderlich, C.H. Bach, and T. Jungwirth, Spin Hall effects, *Rev. Mod. Phys.* **87**, 1213 (2015).
11. A. Hoffmann, Spin Hall effects in metals, *IEEE Trans. Magn.* **49**, 5172 (2013).
12. T. Jungwirth, J. Wunderlich, and O. Kamil, *Nature Mater.* **11**, 382 (2012).
13. A.R. Mellnik, J.S. Lee, A. Richardella, J.L. Grab, P.J. Mintun, M.H. Fischer, A. Vaezi, A. Manchon, E.-A. Kim, N. Samarth, and D.C. Ralph, Spin-transfer torque generated by a topological insulator, *Nature* **511**, 449 (2014).
14. Y. Fan, P. Upadhyaya, X. Kou, M. Lang, S. Takei, Z. Wang, J. Tang, L. He, L.-T. Chang, M. Montazeri, G. Yu, W. Jiang, T. Nie, R.N. Schwartz, Y. Tserkovnyak, and K.L. Wang, Magnetization switching through giant spin-orbit torque in a magnetically doped topological insulator heterostructures, *Nature Mater.* **13**, 699 (2014).
15. I.M. Miron, K. Garello, G. Gaudin, P.-J. Zermatten, M.V. Costache, S. Auffret, S. Bandiera, B. Rodmacq, A. Schuhl, and P. Gambardella, Perpendicular switching of a single ferromagnetic layer induced by in-plane current injection, *Nature* **476**, 189 (2011).
16. L. Liu, T. Moriyama, D.C. Ralph, and R.A. Buhrman, Spin-torque ferromagnetic resonance induced by the spin Hall effect, *Phys. Rev. Lett.* **106**, 036601 (2011).
17. L. Liu, O.J. Lee, T.J. Gudmundsen, D.C. Ralph, and R.A. Buhrman, Current-induced switching of perpendicularly magnetized magnetic layers using spin torque from the spin Hall effect, *Phys. Rev. Lett.* **109**, 096602 (2012).

18. C.-F. Pai, L. Liu, Y. Li, H.W. Tseng, D.C. Ralph, and R.A. Buhrman, Spin transfer torque devices utilizing the giant spin Hall effect in tungsten, *Appl. Phys. Lett.* **101**, 122404 (2012).
19. K. Garello, I.M. Miron, C.O. Avci, F. Freimuth, Y. Mokrousov, S. Blügel, S. Auffret, O. Boulle, G. Gaudin, and P. Gamardella, Symmetry and magnitude of spin-orbit torques in ferromagnetic heterostructures, *Nature Nanotech.* **8**, 587 (2013).
20. G. Yu, P. Upadhyaya, Y. Fan, J.G. Alzate, W. Jiang, K.L. Wong, S. Takei, S.A. Bender, L.-T. Chang, Y. Jiang, M. Lang, J. Tang, Y. Wang, Y. Tserkovnyak, P.K. Amiri, and K.L. Wang, Switching of perpendicular magnetization by spin-orbit torques in the absence of external magnetic fields, *Nature Nanotech.* **9**, 548 (2014).
21. W. Zhang, M.B. Jungfleisch, W. Jiang, J.E. Pearson, A. Hoffmann, F. Freimuth, and Y. Mokrousov, Spin Hall effects in metallic antiferromagnets, *Phys. Rev. Lett.* **113**, 196602 (2014).
22. S. Woo, M. Mann, A.J. Tan, L. Caretta, and G.S.D. Beach, Enhanced spin-orbit torques in Pt/Co/Ta heterostructures, *Appl. Phys. Lett.* **105**, 212404 (2014).
23. S. Fukami, T. Anekawa, C. Zhang, and H. Ohno, A spin-orbit torque switching scheme with collinear magnetic easy axis and current configuration, *Nature Nanotech.* advance online publication, doi:10.1038/nnano.2016.29.
24. W. Zhang. M.B. Jungfleisch, W. Jiang, J.E. Pearson, A. Hoffmann, F. Freimuth, and Y. Mokrousov, All-electrical manipulation of magnetization dynamics in a ferromagnet by antiferromagnets with anisotropic spin Hall effects, *Phys. Rev. B.* **92**, 144405 (2015).
25. S. Fukami, C. Zhang, S. DuttaGupta, A. Kurenkov, and H. Ohno, Magnetization switching by spin-orbit torque in an antiferromagnet-ferromagnet bilayer system, *Nature Mater.* **15**, 535 (2016).
26. I.M. Miron, G. Gaudin, S. Auffret, B. Rodmacq, A. Schuhl, S. Pizzini, J. Vogel, and P. Gambardella, Current-driven spin torque induced by the Rashba effect in a ferromagnetic metal layer, *Nature Mater.* **9**, 230 (2010).
27. I.M. Miron, T. Moore, H. Szambolics, L.D. Buda-Prejbeanu, S. Auffret, B. Rodmacq, S. Pizzini, J. Vogel, M. Bonfim, A. Schuhl, and G. Gaudin, Fast current-induced domain-wall motion controlled by the Rashba effect, *Nature Mater.* **10**, 419 (2011).
28. S. Emori, U. Bauer, S.-M. Ahn, E. Martinez, and G.S.D. Beach, Current-driven dynamics of chiral ferromagnetic domain walls, *Nature Mater.* **12**, 611 (2013).
29. P.P.J. Haazen, E. Murè, J.H. Franken, R. Lavrijsen, H.J.M. Swagten, and B. Koopmans, Domain wall depinning governed by the spin Hall effect, *Nature Mater.* **12**, 299 (2013).
30. A. van der Brink, G. Vermijs, A. Solignac, J. Koo, J.T. Kohlhepp, H.J.M. Swagten, and B. Koopmans, Field-free magnetization reversal by spin-Hall effect and exchange bias, *Nature Comms.* **7**, 10854 (2016).
31. C.K. Safeer, E. Jué, A. Lopez, L. Buda-Prejbeanu, S. Auffret, S. Pizzini, O. Boulle, I.M. Miron, and G. Gaudin, Spin-orbit torque magnetization switching controlled by geometry, *Nature Nanotech.* **11**, 143 (2016).
32. M.R. Scheinfein, J. Unguris, M.H. Kelley, D.T. Pierce, & R.J. Celotta, Scanning electron microscopy with polarization analysis (SEMPA). *Rev. Sci. Instrum.* **61,** 2501 (1990).
33. R. Allenspach, in *Modern Techniques for Characterizing Magnetic Materials*, edited by Y. Zhu (Kluwer Academic Publishers, Boston, 2005).
34. T. Kohashi and K. Koike, A spin-polarized scanning electron microscope with 5-nm resolution, *Jpn. J. Appl. Phys.* **40**, L1264 (2001).

35. R.P. Cowburn, Property variation with shape in magnetic nanoelements, *J. Phys. D: Appl. Phys.* **33**, R1 (2000).
36. W. Jiang, P. Upadhyaya, W. Zhang, G. Yu, M.B. Jungfleisch, F.Y. Fradin, J.E. Pearson, Y. Tserkovnyak, K.L. Wang, O. Heinonen, S.G.E. te Velthuis, and A. Hoffmann, Blowing magnetic skyrmion bubbles, *Science* **349**, 283 (2015).
37. S. Ikeda, K. Miura, H. Yamamoto, K. Mizunuma, H.D. Gan, M. Endo, S. Kanai, J. Hayakawa, F. Matsukura, and H. Ohno, A perpendicular-anisotropy CoFeB-MgO magnetic tunnel junction, *Nature Mater.* **9**, 721 (2010).
38. D.C. Worledge, G. Hu, D.W. Abrabam, P.L. Trouilloud, and S. Brown, Development of perpendicularly magnetized Ta/CoFeB/MgO-based tunnel junctions at IBM, *J. Appl. Phys.* **115**, 172601 (2014).
39. T. VanZandt, R. Browning, and M. Landolt, Iron overlayer polarization enhancement technique for spin-polarized electron microscopy, *J. Appl. Phys.* **69**, 1564 (1991).
40. C.-F. Pai, M.-H. Nguyen, C. Belvin, L.H. Vilela-Leão, D.C. Ralph, and R.A. Buhrman, Enhancement of perpendicular magnetic anisotropy and transmission of spin-Hall-effect-induced spin currents by a Hf spacer layer in W/Hf/CoFeB/MgO layer structures, *Appl. Phys. Lett.* **104**, 082407 (2014).
41. M.-H. Nguyen, D.C. Ralph, and R.A. Buhrman, Spin torque study of the spin Hall conductivity and spin diffusion length in platinum thin films with varying resistivity, *Phys. Rev. Lett.* **116**, 126601 (2016).
42. S.V. Aradhya, G.E. Rowlands, J. Oh, D.C. Ralph, and R.A. Buhrman, Nanosecond-timescale low error switching of in-plane magnetic tunnel junctions through dynamic Oersted-field assisted spin-Hall effect, preprint at http://arxiv.org/abs/1605.02104.
43. K.-S. Ryu, L. Thomas, S.-H. Yang, and S. Parkin, Chiral spin torque at magnetic domain walls, *Nature Nanotech.* **8**, 527 (2013).
44. S.S.P. Parkin, M. Hayashi, and L. Thomas, Magnetic domain-wall racetrack memory, *Science* **320**, 190 (2008).
45. S. Woo, K. Litzius, B. Krüger, M.-Y. Im, L. Caretta, K. Richter, M. Mann, A. Krone, R.M. Reeve, M. Weigand, P. Agrawal, I. Lemesh, M.-A. Mawass, P. Fischer, M. Kläui, and G.S.D. Beach, Observation of room-temperature magnetic skyrmions and their current-driven dynamics in ultrathin metallic ferromagnets, *Nature Mater.* **15**, 501 (2016).

FIGURES

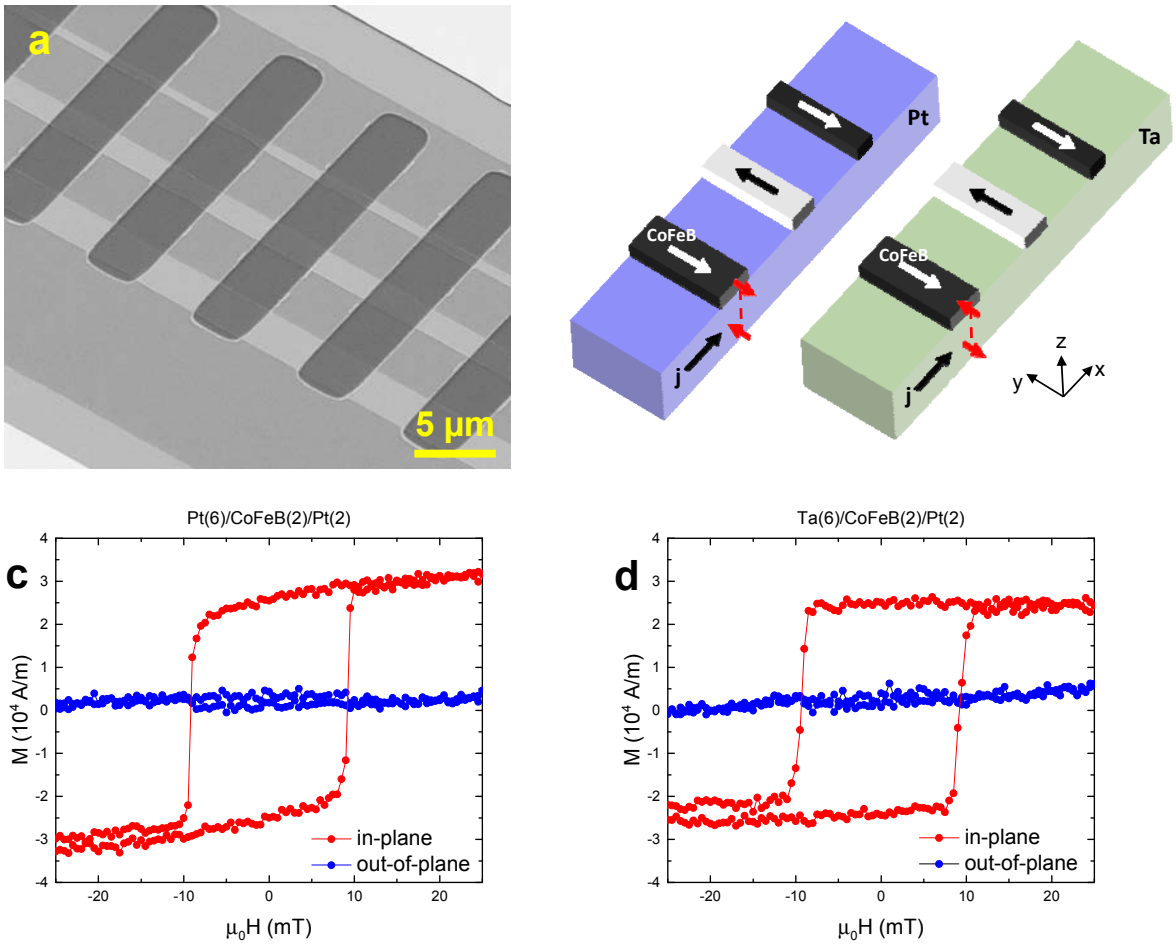

Figure 1. (a) A scanning electron micrograph of one of the devices studied in this work. The bright regions in the upper right and lower left corners are Au contact pads. Between the contact pads are 4 μm wide Ta strips with transverse CoFeB (lighter contrast) rectangles on top. (b) Sample geometry for direct imaging of in-plane magnetization reversal driven by spin-orbit torque. Rectangles of CoFeB (shaded black or white depending on the magnetization orientation, as in SEMPA images) are fabricated on top of strips of Pt or Ta. When a current pulse is sent through a strip, a transverse spin current (represented by the dashed red lines and arrows) is generated by the spin orbit torque of the heavy metal. The spin currents generated in Pt and Ta are opposite: a current pulse in the +x direction will rotate the CoFeB magnetization to the –y direction for the Pt sample, but the same pulse in the Ta sample will rotate the CoFeB magnetization to the +y direction. Panels (c) and (d) show in-plane and out-of-plane vibrating sample magnetometry hysteresis loops for unpatterned witness films of Pt(6)/CoFeB(2)/Pt(2) and Ta(6)/CoFeB(2)/Pt(2), respectively, demonstrating the in-plane easy axis. Uncertainties are derived from the uncertainty from the VSM and are smaller than the data markers.

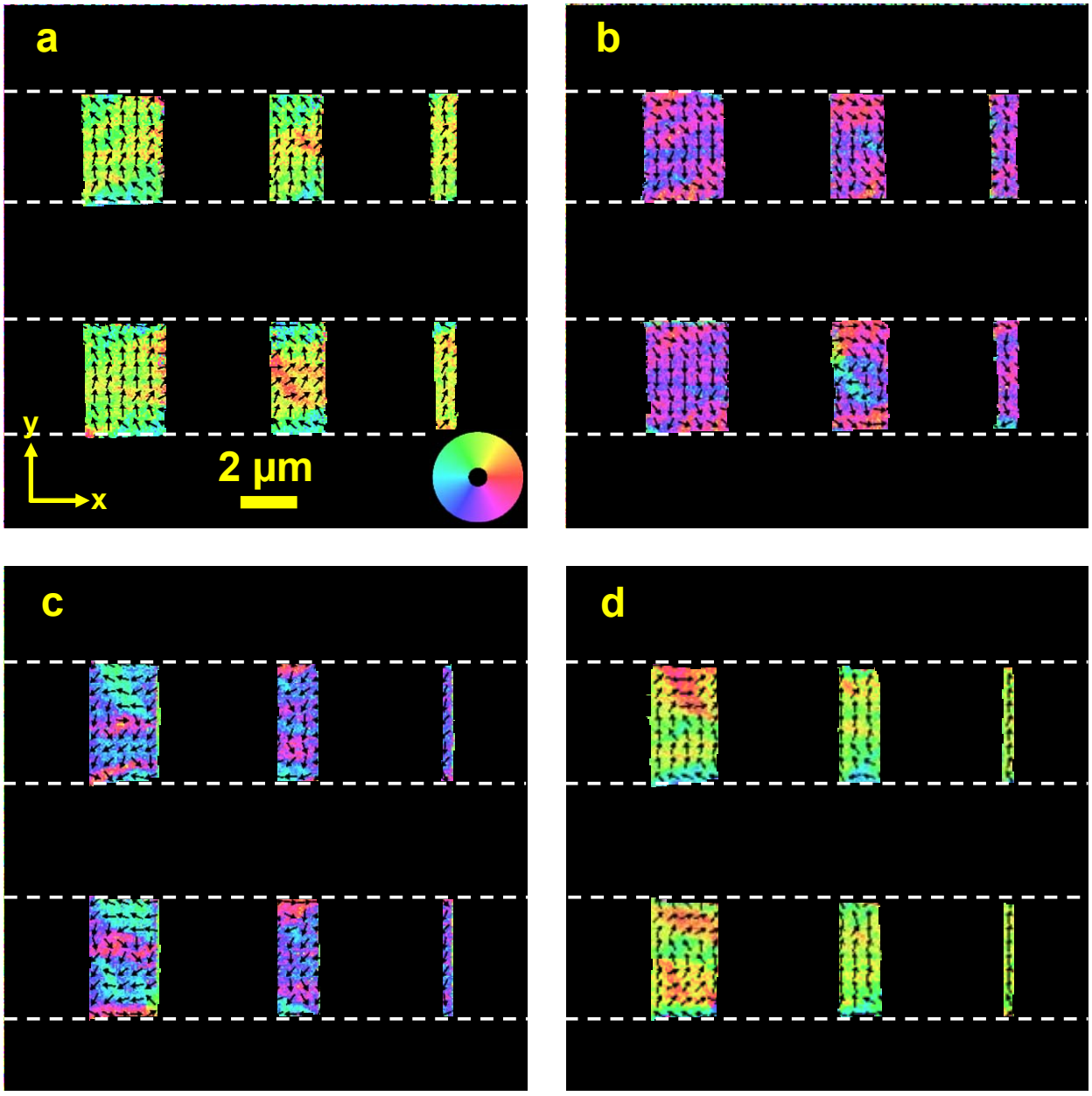

Figure 2. SEMPA images of in-plane magnetization reversal driven by the spin-orbit torques of Pt and Ta**.** The magnetization direction is indicated by the color wheel inset in (a) and by small black arrows, and the edges of the heavy metal strips are indicated by the dashed lines. The top two panels show the magnetization of CoFeB rectangles on top of Pt strips before (a) and after (b) a 0.3 µs, 4×10^{12} A/m^2 current pulse in the +x direction. The magnetization is switched from the +y direction to the –y direction [axes indicated in (a)]. The bottom two panels show the magnetization of CoFeB rectangles on top of Ta strips before (c) and after (d) a 0.3 µs, 1×10^{12} A/m^2 current pulse in the +x direction. In this case, the magnetization is switched from the –y direction to the +y direction, opposite the direction of the switching seen with the Pt strips.

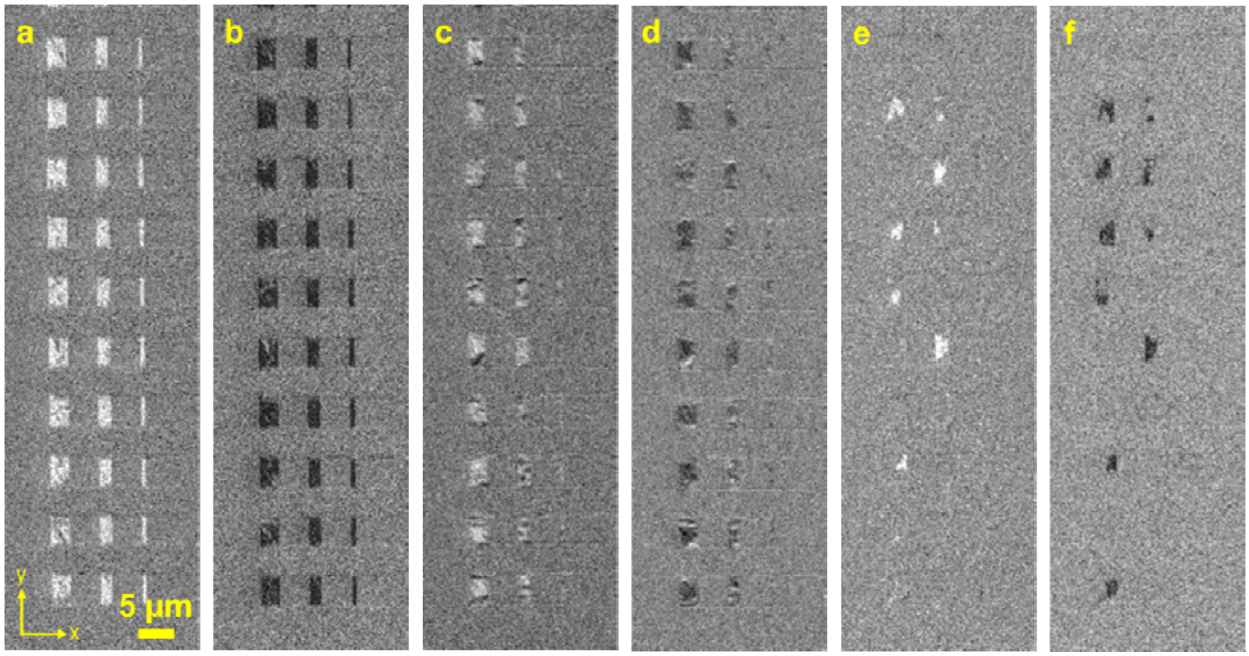

Figure 3. Simultaneous measurement of magnetization reversal in 30 different CoFeB rectangles (on Ta strips). These figures are difference images generated by subtracting subsequent SEMPA images of one of the magnetization components from each other. White contrast represents magnetization that has reversed from –y (–x) to +y (+x), black contrast represents magnetization that has reversed from +y (+x) to –y (–x), and gray contrast represents nonmagnetic areas as well as regions in which the magnetization did not change between images. Panels (a) and (b) show changes in the y-component magnetization after 8×10^{11} A/m^2 current pulses in the +x and –x directions, respectively. Panels (c) and (d) show the corresponding changes in the x-component magnetization. Panels (e) and (f) show the y-component magnetization after slightly smaller 6×10^{11} A/m^2 current pulses in the +x and –x directions, respectively. Here the spin-orbit torque is weaker and can only reverse some of the magnetization in the wider CoFeB rectangles.

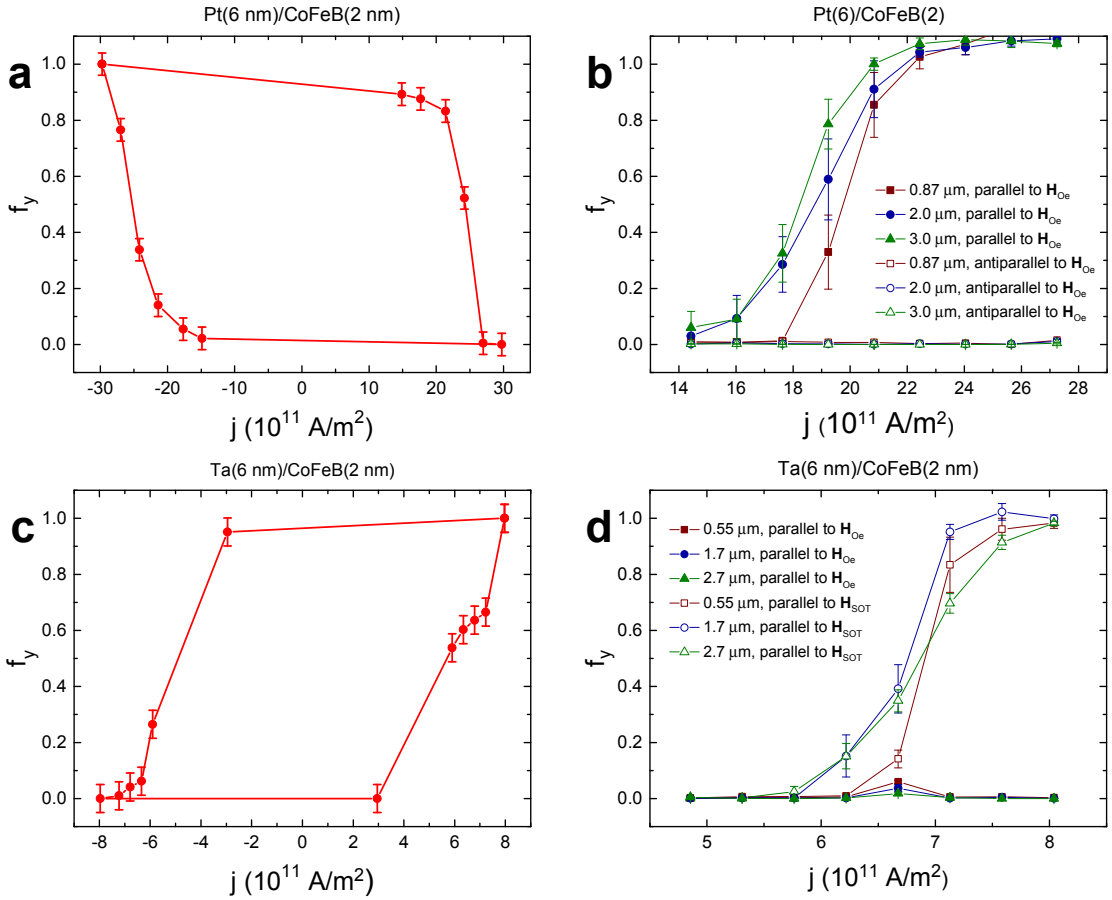

Figure 4. (a) The fraction of the y-component of CoFeB magnetization reversed (f_y) vs. current density for the 2.0 × 4.0 μm CoFeB rectangles on Pt strips. The open loop shows clear deterministic and reversible spin-orbit torque-driven magnetization reversal in zero applied magnetic field. (b) The magnitude of f_y vs. current density for all three sizes of CoFeB rectangles (averaged over switching from +y to -y and vice versa). Filled symbols indicate switching with the symmetry expected from the spin-orbit torque and Oersted field (which are the same for the case of Pt), and open symbols indicate switching with the opposite symmetry. The critical currents extracted from these data are presented in Supplementary Tables 1 and 2. Panels (c) and (d) show analogous data for the Ta/CoFeB sample. In this case, the spin-orbit torque and the Oersted field have opposite symmetries, and the observed switching symmetry is consistent with the spin-orbit torque (open symbols) and not the Oersted field (filled symbols). Vertical bars indicate single standard uncertainties determined by the standard deviations of all 10 elements measured for each size.